



Photocatalytic performance enhanced via surface bismuth vacancy of $\text{Bi}_6\text{S}_2\text{O}_{15}$ core/shell nanowires



Jun Wang, Wenjun Jiang, Di Liu, Zhen Wei, Yongfa Zhu*

Department of Chemistry, Tsinghua University, Beijing 100084, PR China

ARTICLE INFO

Article history:

Received 23 February 2015

Received in revised form 8 April 2015

Accepted 10 April 2015

Available online 13 April 2015

Keywords:

Surface bismuth vacancy

Photocatalytic

$\text{Bi}_6\text{S}_2\text{O}_{15}$ core/shell nanowires

ABSTRACT

Core/shell structured $\text{Bi}_6\text{S}_2\text{O}_{15}$ nanowires with surface bismuth defects are fabricated via a one-step hydrothermal method. The UV photocatalytic activity of the defective $\text{Bi}_6\text{S}_2\text{O}_{15}$ nanowires is about 4 times as high as that of pure $\text{Bi}_6\text{S}_2\text{O}_{15}$ nanowires. The light response range of $\text{Bi}_6\text{S}_2\text{O}_{15}$ nanowires is greatly expanded from 370 nm to 450 nm via surface bismuth-vacancy. The main oxidative species transform from holes (h^+) to the superoxide radical ($\bullet\text{O}_2^-$) and hydroxyl radicals ($\bullet\text{OH}$) owing to the great changes of the electronic structure of vacancy $\text{Bi}_6\text{S}_2\text{O}_{15}$. Surface bismuth vacancies elevate the conduction band (CB) and introduce impurity states above the valence band (VB) of $\text{Bi}_6\text{S}_2\text{O}_{15}$. The higher potential of CB benefits for the production of superoxide radical ($\bullet\text{O}_2^-$) and the hydroxyl radicals is result from the surface hydroxide radical defects formed with the introduction of surface bismuth-vacancy. The enhancement in photocatalytic performance is attributed to the high separation efficiency of photoinduced electron-hole pairs due to the broadening of the valence band (VB), and the extending of photoresponse is result from the narrowing of energy band gap owing to the rise of the valence band maximum (VBM).

© 2015 Elsevier B.V. All rights reserved.

1. Introduction

Photocatalytic materials have received enormous attention in the past decades, owing to its extensive applications in photocatalysis for water and air purification, solar cells, hydrogen energy production, and more [1–3]. However, the practical applications of photocatalytic technique are greatly restricted by the high recombination probability of the electron-hole pairs and narrow light-response range [4]. Understanding and tailoring the electronic structure of semiconductor is considered to be an avenue to overcome these serious drawbacks of photocatalytic materials. Indeed, a suitable value of the band gap is a crucial requirement for optimizing semiconductor solar light conversion capability [5]. Typical band gap engineering involves metal or nonmetal impurities doping [6,7]. However, bulk defects introduced by dopants can only act as charge traps and recombination centers, resulting in the decrease of photoactivity efficiency [8]. Theoretical and experimental studies clearly demonstrate that, compared to bulk defects, surface defects serve as photoinduced charge traps as well as adsorption sites where the charge transfer to adsorbed species can prevent the electron-hole recombination in bulk, which is conducive to

the improvement of photocatalytic activity [9,10]. Recently, Naldoni et al. synthesized defective core/disordered shell black TiO_2 NPs with a reduced band gap of only 1.85 eV via a one-step crystallization/reduction process, which exhibits a broad absorption, starting at ~ 400 nm and extending in the near-infrared (NIR) region of the spectrum [11]. In our previous work, the introduction of surface oxygen vacancies in several semiconductors (ZnO and BiPO_4) is demonstrated to be conducive to band gap narrowing and photoactivity [12–14]. Cited examples show the decisive role of surface oxygen vacancies in electronic structure tailored and photoactivity enhancement. However, the effect of surface cation defects in electronic structure and photocatalysis have rarely been reported. The main text of this article should go here with headings as appropriate.

Herein, the photocatalytic, structural, and electronic properties of novel surface bismuth defects core-shell $\text{Bi}_6\text{S}_2\text{O}_{15}$ nanowires were elucidated. The UV photocatalytic activity of the vacancy $\text{Bi}_6\text{S}_2\text{O}_{15}$ nanowires is about 4 times as high as that of pure $\text{Bi}_6\text{S}_2\text{O}_{15}$ nanowires. Thickness of bismuth defects shell can be simply tuned by increasing the molar ratios of SO_4^{2-} to Bi^{3+} , in which the $[\text{BiO}_6]$ with only Bi–O–Bi bonds in surface crystal transform into the $[\text{BiO}_3]$ with Bi–O–Bi and Bi–O–S bonds. Surface bismuth vacancies elevate the conduction band (CB) about 0.34 eV and introduce impurity states above the valence band (VB). The new electronic state reduces the surface band gap by 0.59 eV. As a result, the

* Corresponding author. Tel.: +86 10 62787601; fax: +86 10 62787601.
E-mail address: zhuyf@tsinghua.edu.cn (Y. Zhu).

dramatic visible photocatalytic activity is generated due to the narrowing of energy band gap with the introduction of surface bismuth-vacancy. And the main oxidative species of photocatalysts are demonstrated to transform from holes (h^+) to the superoxide radical ($\cdot O_2^-$) and hydroxyl radicals ($\cdot OH$). The enhancement in photocatalytic performance is attributed to the high separation efficiency of photoinduced electron–hole pairs owing to the broadening of the valence band (VB).

2. Experimental

2.1. Preparation of pure and vacancy $Bi_6S_2O_{15}$ nanowires photocatalysts

All chemicals used were analytic grade reagents without further purification. Bismuth nitrate ($Bi(NO_3)_3 \cdot 5H_2O$), Sodium sulfate (Na_2SO_4), 25–28% Ammonia (25–28% $NH_3 \cdot H_2O$) were purchased from Beijing Chemical Works (Beijing, China).

2.1.1. Synthesis of pure $Bi_6S_2O_{15}$ nanowires

In a typical procedure, 0.67 mmol Na_2SO_4 and 2 mmol $Bi(NO_3)_3 \cdot 5H_2O$ (1:3 molar ratio) were mixed together, and then 30 mL of distilled water and 0.5 mL 25–28% $NH_3 \cdot H_2O$ were added. The concentration of precursors were about 0.022 M and 0.067 M for the Na_2SO_4 and $Bi(NO_3)_3 \cdot 5H_2O$, respectively. The resulting precursor suspension was magnetically stirred for 30 min at room temperature and then transferred into a 40 mL Teflon-lined stainless steel autoclave. The autoclave was sealed and maintained at 180 °C for 24 h in a digital oven, without shaking or stirring, then allowed to cool naturally to room temperature. The white precipitate was washed with distilled water, three times. Then, it was dried at 60 °C in air. The product yields was about 0.64 g.

2.1.2. Synthesis of vacancy $Bi_6S_2O_{15}$ nanowires

In a typical procedure, 6 mmol Na_2SO_4 and 2 mmol $Bi(NO_3)_3 \cdot 5H_2O$ (3:1 molar ratio) were mixed together, and then 30 mL of distilled water and 0.5 mL 25–28% $NH_3 \cdot H_2O$ were added. The concentration of precursors were about 0.2 M and 0.067 M for the Na_2SO_4 and $Bi(NO_3)_3 \cdot 5H_2O$, respectively. The resulting precursor suspension was magnetically stirred for 30 min at room temperature and then transferred into a 40 mL Teflon-lined stainless steel autoclave. The autoclave was sealed and maintained at 180 °C for 24 h in a digital oven, without shaking or stirring, then allowed to cool naturally to room temperature. The white precipitate was washed with distilled water, three times. Then, it was dried at 60 °C in air. The product yields was about 0.77 g. The thickness of vacancy can be controlled by tuning the molar ratio of Na_2SO_4 to $Bi(NO_3)_3 \cdot 5H_2O$.

2.1.3. Preparation of the electrodes

Five milligram of as-prepared photocatalyst was suspended in 0.5 mL of distilled water to produce slurry, which was then dip-coated onto a 2 cm \times 4 cm indium–tin oxide (ITO) glass electrode. Electrodes were exposed to air for 24 h to remove water and subsequently calcined at 150 °C for 5 h.

2.2. Characterizations

The products were characterized by powder X-ray diffraction (XRD) on a Bruker D8-advance X-ray diffractometer at 40 kV and 40 mA for monochromatized Cu $K\alpha$ (λ) 1.5418 Å radiation. Morphologies and structures of the prepared samples were further examined with LEO-1530 field emission scanning electron microscope (SEM) and JEM 1200 transmission electron microscopy (TEM). HRTEM images were obtained with a JEM 2010F field

emission gun transmission electron microscope operated at an accelerating voltage of 200 kV. Raman spectra were recorded on a microscopic confocal Raman spectrometer (Renishaw 1000 NR) with an excitation of 514.5 nm laser light. Fourier transform infrared (FTIR) spectra were carried out using Bruker V70FTIR spectrometer in the frequency range of 4000–600 cm^{-1} with a resolution of 4 cm^{-1} . The Brunauer–Emmett–Teller (BET) surface area was measured by ASAP2010V5.02H. The absorbed gas was nitrogen. Diffuse reflection spectra (DRS) were obtained on a Hitachi U-3010 UV–vis spectrophotometer. $BaSO_4$ was used as the reflectance standard in the experiment. Chemical characterization of the sample surface was recorded with X-ray photoelectron spectroscopy (XPS ULVAC-PHI, Quantera). The charge effect was calibrated using the binding energy of C 1s. The photocurrent and electrochemical impedance spectroscopy (EIS) were measured on an electrochemical system (CHI-660B, China). UV light 254 nm was obtained from an 11 W germicidal lamp (Institute for Electric Light Sources, Beijing). A standard three electrode cell with ITO/pure $Bi_6S_2O_{15}$ nanowires or ITO/vacancy $Bi_6S_2O_{15}$ nanowires as a working electrode, a platinum wire as a counter electrode, and a standard calomel electrode (SCE) as reference electrode were used in photoelectric studies. 0.1 M Na_2SO_4 was used as the electrolyte solution. Potentials were given with reference to the SCE. The photoelectric responses of the photocatalysts as light on and off were measured at 0.0 V. Total organic carbon analyzer (analytikjenaA, MultiN/C2100TOC/TN) was employed for mineralization degree analysis of MB solutions.

2.3. Catalytic evaluation

The photocatalytic activities of the as-prepared samples were evaluated by the decomposition of methylene blue (MB) in solution under UV and visible light. The UV light source was obtained by a 15 W UV germicidal lamp ($\lambda = 254$ nm), and the average light intensity was 0.79 $mW\ cm^{-2}$. An amount of 15 mg of photocatalyst was added into prepared 50 mL of 1×10^{-5} M MB aqueous solution. Before the light irradiation, the suspensions were first ultrasonic dispersed in dark for 15 min and then magnetically stirred for 15 min to reach the absorption–desorption equilibrium. At given time intervals, 2.7 mL aliquots were sampled and centrifuged to remove the photocatalyst particles. Synchronously, the filtrates of MB solutions at different conditions were analyzed by recording variations of the maximum absorption peak 663 nm in the UV–vis spectra using a Hitachi U-3010 UV–vis spectrophotometer. Total organic carbon analyzer of the as-prepared samples was evaluated by decomposition of 50 mL of 1×10^{-5} M MB and 10 ppm phenol solution under UV light.

3. Results and discussion

3.1. Photocatalytic activity of surface bismuth defects $Bi_6S_2O_{15}$ nanowires

The photocatalytic activities of the pure and vacancy $Bi_6S_2O_{15}$ nanowires are evaluated by the photodegradation of MB and phenol in solution under UV light irradiation ($\lambda = 254$ nm). The first-order linear relationship is revealed by the plots of the $\ln(C/C_0)$ vs. irradiation time (t), where C is the concentration of MB or phenol at the irradiation time t and C_0 is the concentration in the adsorption equilibrium of the photocatalysts before irradiation. Fig. 1A shows the photocatalytic activities of pure and vacancy $Bi_6S_2O_{15}$ nanowires on the degradation of MB. The blank test was also performed to investigate the self-sensitized degradation of MB. The result shows that only about 1.8% of MB have been degraded under the UV light after 80 min. The photocatalytic reaction-rate

obviously increases after introducing the photocatalysts. It is clear that the vacancy $\text{Bi}_6\text{S}_2\text{O}_{15}$ shows the higher photocatalytic activity than pure $\text{Bi}_6\text{S}_2\text{O}_{15}$. The determined reaction-rate constants k are 3.11×10^{-2} and $0.63 \times 10^{-2} \text{ min}^{-1}$ for vacancy and pure $\text{Bi}_6\text{S}_2\text{O}_{15}$ nanowires photocatalysts, respectively (Fig. 1A inset). The photocatalytic activity of the vacancy $\text{Bi}_6\text{S}_2\text{O}_{15}$ nanowires is about 5 times as high as that of pure $\text{Bi}_6\text{S}_2\text{O}_{15}$. Further investigation on the decomposition of phenol (Fig. 1B) also shows that the vacancy $\text{Bi}_6\text{S}_2\text{O}_{15}$ sample exhibits obviously higher photocatalytic activity than pure $\text{Bi}_6\text{S}_2\text{O}_{15}$. The apparent reaction rate k is estimated to be as high as $0.83 \times 10^{-2} \text{ min}^{-1}$ and the activity increased up to 4 times for the pure $\text{Bi}_6\text{S}_2\text{O}_{15}$ nanowires ($0.20 \times 10^{-2} \text{ min}^{-1}$). The typical HPLC spectrums of phenol solution degraded by vacancy $\text{Bi}_6\text{S}_2\text{O}_{15}$ sample is shown in Fig. S1. Several spectrum peaks appear at low retention time can be attributed to intermediate products of phenol oxidation. Furthermore, the removal of TOC in the photodegradation of MB and phenol has been performed to investigate the mineralization property of the as-prepared photocatalysts (Fig. 1C). It is clear that the removal of TOC obviously increases both in the photodegradation of MB and phenol after introducing the surface vacancy. The TOC removal percentage is about 60% and 35%

for MB and phenol over vacancy $\text{Bi}_6\text{S}_2\text{O}_{15}$ nanowires after 80 min photocatalytic reaction. Therefore, the mineralization ability of vacancy $\text{Bi}_6\text{S}_2\text{O}_{15}$ nanowires is evidently enhanced. In addition, the photocurrent responses of pure and vacancy $\text{Bi}_6\text{S}_2\text{O}_{15}$ nanowires electrodes, under UV light ($\lambda = 254 \text{ nm}$), are provided in Fig. 1D. A fast and stable photocurrent response is observed for each switch-on and switch-off event in both electrodes. The vacancy $\text{Bi}_6\text{S}_2\text{O}_{15}$ nanowires shows a noticeable higher photocurrent. The photocurrent response of vacancy $\text{Bi}_6\text{S}_2\text{O}_{15}$ nanowires electrodes is about 7 times as high as that of pure $\text{Bi}_6\text{S}_2\text{O}_{15}$ nanowires. The result is in accord with the photocatalytic activity of the as-prepared samples. The enhancement of photocurrent indicates that the separation efficiency of photoinduced electron–hole pairs is improved. Based on the results above, it can be concluded that the photocatalytic activity and mineralization property of as-prepared $\text{Bi}_6\text{S}_2\text{O}_{15}$ nanowires photocatalyst can be greatly improved by introducing the surface vacancy.

More interestingly, the spectral response of as-prepared catalyst is greatly expanded with the introduction of surface bismuth-vacancy. The UV–vis diffuse reflectance spectra (DRS) show that the onset of the absorption edge of pure $\text{Bi}_6\text{S}_2\text{O}_{15}$ is about 370 nm,

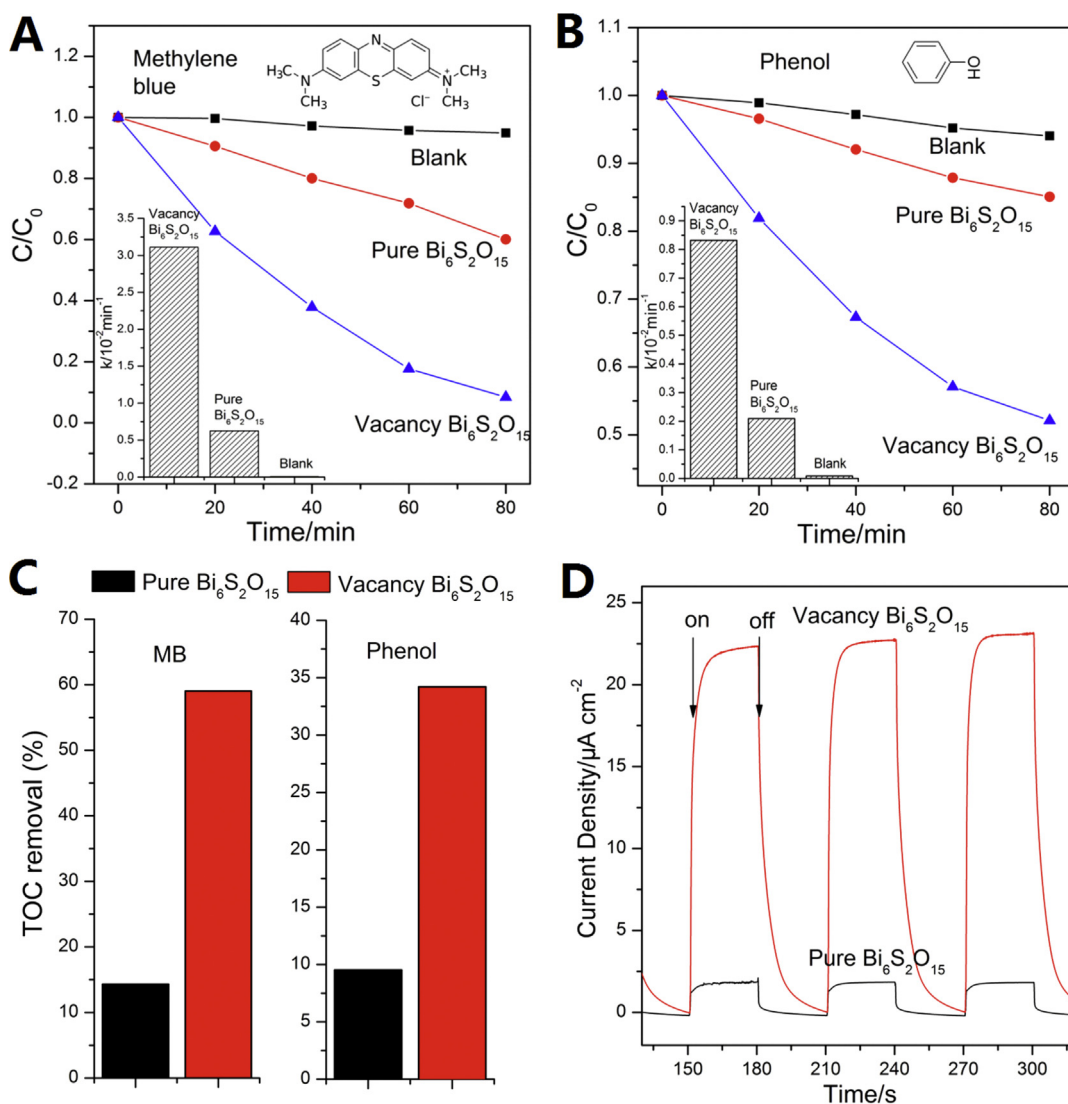


Fig. 1. (A) Photocatalytic degradation of MB over pure $\text{Bi}_6\text{S}_2\text{O}_{15}$ and vacancy $\text{Bi}_6\text{S}_2\text{O}_{15}$ nanowires photocatalysts under the UV light ($\lambda = 254 \text{ nm}$); (B) Degradation rate constant k of pure $\text{Bi}_6\text{S}_2\text{O}_{15}$ and vacancy $\text{Bi}_6\text{S}_2\text{O}_{15}$ nanowires photocatalysts. (C) Photocurrents of pure $\text{Bi}_6\text{S}_2\text{O}_{15}$ and vacancy $\text{Bi}_6\text{S}_2\text{O}_{15}$ nanowires electrodes under UV light irradiation. (D) TOC removal plots of MB over pure $\text{Bi}_6\text{S}_2\text{O}_{15}$ and vacancy $\text{Bi}_6\text{S}_2\text{O}_{15}$ nanowires photocatalysts.

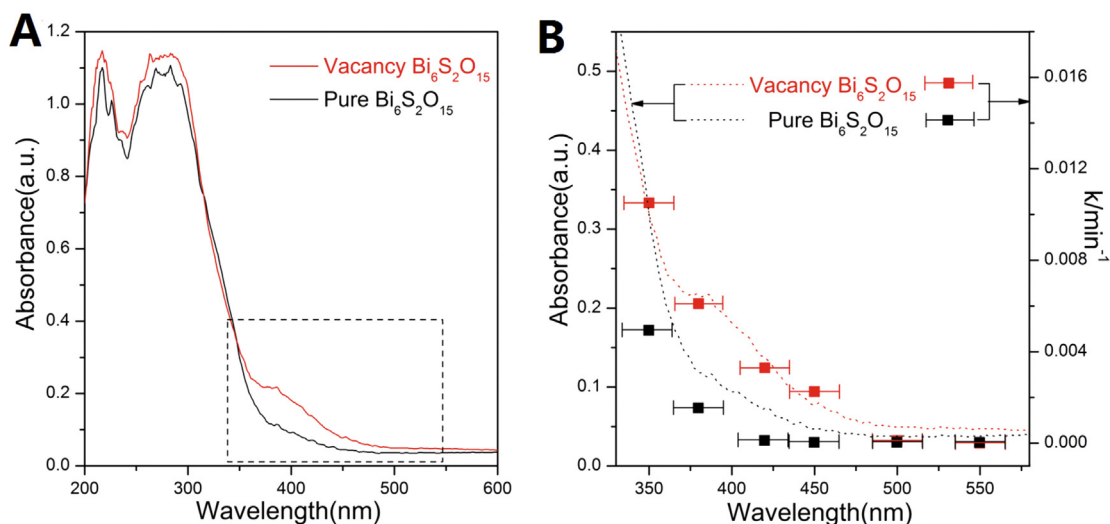


Fig. 2. (A) UV-vis diffuse reflectance spectra of pure $\text{Bi}_6\text{S}_2\text{O}_{15}$ and vacancy $\text{Bi}_6\text{S}_2\text{O}_{15}$ nanowires. (B) Wavelength-dependent MB degradation by vacancy $\text{Bi}_6\text{S}_2\text{O}_{15}$ nanowires.

corresponding to the band gap of 3.35 eV (shown in Fig. 2A). Compared with pure $\text{Bi}_6\text{S}_2\text{O}_{15}$ nanowires, the main absorption edge and highest absorption peak of vacancy $\text{Bi}_6\text{S}_2\text{O}_{15}$ nanowires has hardly any change. However, the absorbance of vacancy $\text{Bi}_6\text{S}_2\text{O}_{15}$ nanowires is enhanced in the range of 370–500 nm, which may be induced by surface vacancies as it generally does in TiO_2 [5], ZnO [12], and BiPO_4 [15]. In addition, the wavelength-dependent MB degradation over pure $\text{Bi}_6\text{S}_2\text{O}_{15}$ and vacancy $\text{Bi}_6\text{S}_2\text{O}_{15}$ nanowires are also examined as shown in Fig. 2B. The trends of MB degradation rates over both two catalysts match well with that of absorption in the optical spectra. Note that the vacancy $\text{Bi}_6\text{S}_2\text{O}_{15}$ nanowires could hardly be excited by visible light (>420 nm), while the longest wavelength available for the reaction over the vacancy $\text{Bi}_6\text{S}_2\text{O}_{15}$ nanowires can reach 450 nm. These results indicate that the dramatic visible photocatalytic activity are generated due to the introducing of surface bismuth-vacancy.

It is well known that the concentration of vacancies play a critical role in determining the photocatalytic performance of a catalyst [15]. In our work, the vacancies concentration can be represented by the thickness of defect layer, which can be simply tuned by increasing the molar ratios of SO_4^{2-} to Bi^{3+} in the precursor. The UV photocatalytic activities of pure $\text{Bi}_6\text{S}_2\text{O}_{15}$ and vacancy $\text{Bi}_6\text{S}_2\text{O}_{15}$ nanowires synthesized with various molar ratios of SO_4^{2-} to Bi^{3+} on the degradation of MB are investigated. As shown in Fig. 3, the photocatalytic activities of vacancy $\text{Bi}_6\text{S}_2\text{O}_{15}$ nanowires samples gradually enhanced with the increase of the molar ratios of SO_4^{2-} to Bi^{3+} . When the molar ratios of SO_4^{2-} to Bi^{3+} is 3.0, the vacancy $\text{Bi}_6\text{S}_2\text{O}_{15}$ nanowires displays the highest photocatalytic activity. Further increasing the molar ratios of SO_4^{2-} to Bi^{3+} , however, the degradation rate decreases. The corresponding photocurrent responses of pure $\text{Bi}_6\text{S}_2\text{O}_{15}$ and vacancy $\text{Bi}_6\text{S}_2\text{O}_{15}$ nanowires electrodes, under UV light ($\lambda = 254$ nm), are provided in Fig. S2. It is found that all of the vacancy $\text{Bi}_6\text{S}_2\text{O}_{15}$ nanowires electrodes show the higher photocurrent response than pure $\text{Bi}_6\text{S}_2\text{O}_{15}$ nanowires electrode. The enhancement/decrease of photocurrent is in accord with the photocatalytic activity of the as-prepared samples.

The morphology of as-prepared samples are examined by the TEM in order to check the thickness of defect shells. The results are shown in Fig. S3 and the detail information is summarized in Table S1. It is found that the diameter of nanowires slightly decreases as the molar ratio of SO_4^{2-} to Bi^{3+} increases. And the defect shell of nanowires tend to form at the higher molar ratios of SO_4^{2-} to Bi^{3+} . When the molar ratios of SO_4^{2-} to Bi^{3+} are lower than 1.0 (1:3 and 1:1), no obvious defect shell can be found in our experiments (Fig.

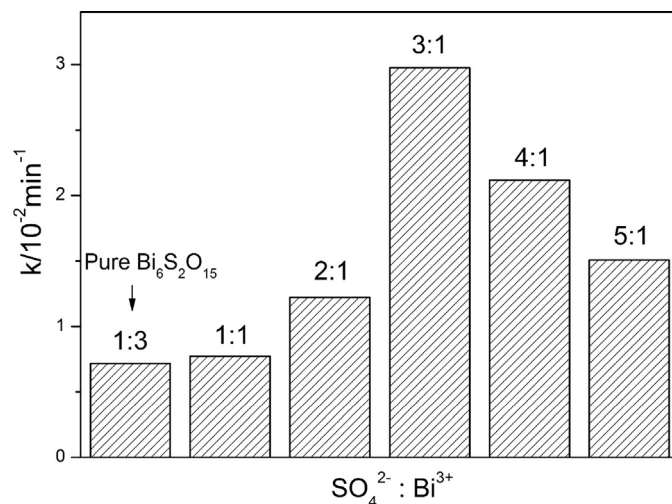


Fig. 3. The rate constant k of $\text{Bi}_6\text{S}_2\text{O}_{15}$ photocatalysts synthesized with various molar ratios of SO_4^{2-} to Bi^{3+} on the degradation of MB ($\lambda = 254$ nm).

S3A and B). The thickness of defect shell is about 3.5 nm when the molar ratio is 2.0 (Fig. S3C). Further increasing the concentration of SO_4^{2-} , the defect shell became thicker. The thickness of defect shells are about 5.1, 8.9, and 9.7 nm at 3.0, 4.0, and 5.0 molar ratios of SO_4^{2-} to Bi^{3+} (Fig. S3D–F).

To further understand the role of surface vacancies in photocatalysis, the relationship between surface defect shell and photocatalytic activity results of $\text{Bi}_6\text{S}_2\text{O}_{15}$ nanowires synthesized for various molar ratio of SO_4^{2-} to Bi^{3+} is summarized as shown in Fig. 4. When the surface defect shell is too thin, the photocatalytic activity only improves slightly and enhances gradually with the increase of the thickness of surface defect shell; while the surface defect shell is too thick, the photocatalytic activity of as-prepared samples decrease significantly. As mentioned above, the diameter of nanowires slightly decrease as the molar ratio of SO_4^{2-} to Bi^{3+} increases. In general, the smaller size of nanoparticle, the higher the efficiency of charge separation, which results in the improvement of photocatalytic activity. However, it is noted that activity decreasing order is just opposite to diameter of vacancy $\text{Bi}_6\text{S}_2\text{O}_{15}$ nanowires when the surface defect shell is too thick. Further investigation on the BET surface area of as-prepared samples shows that there is no changes in order-of-magnitude (Table S2).

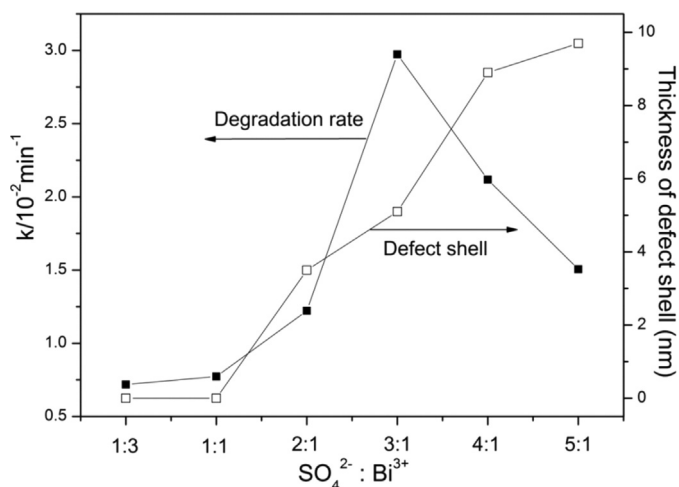


Fig. 4. Defect-dependent MB degradation by vacancy Bi₆S₂O₁₅ nanowires.

These obtained results indicate that the morpholog and physical adsorption characterizations of Bi₆S₂O₁₅ nanowires synthesized for various molar ratio of SO₄²⁻ to Bi³⁺ may play little role in their photocatalytic reaction. Thus, we tentatively conjecture that the decrease of photocatalytic activity is result from the bulk vacancies generated when the surface defect shell is too thick, which may be the recombination center of electron–hole pairs. Based on the discussed above, the surface defect shell controlled by tuning the molar ratio of SO₄²⁻ to Bi³⁺ plays an important role in improving the photocatalytic activity of Bi₆S₂O₁₅ nanowires.

It is well known that the stability and repeatable usability of semiconductors are important parameters to measure their practical value. To conform the stability and reusability of the vacancy Bi₆S₂O₁₅ photocatalyst, repeated runs for the photocatalytic degradation of MB were carried out as shown in Fig. 5A. It is found that the photocatalytic activity do not decrease significantly after four successive cycles. Furthermore, the catalyst's activity was maintained effectively after storage for 4 months (Fig. 5B). The results demonstrated that the vacancy Bi₆S₂O₁₅ nanowires is stable during the photodegradation test.

3.2. Cation-deficient structure in surface bismuth defects core-shell Bi₆S₂O₁₅ nanowires

The crystalline structures of the pure Bi₆S₂O₁₅ and vacancy Bi₆S₂O₁₅ nanowires samples are determined by X-ray diffraction (Fig. S4). The diffraction peaks of the as-prepared samples are in good agreement with the previous report of Bi₆S₂O₁₅ nanowires ($a = 12.206(1) \text{ \AA}$, $b = 19.611(2) \text{ \AA}$, $c = 5.8388(7) \text{ \AA}$; SG Ccc2) [16]. No transformation or any impurity is observed. A unit cell of Bi₆S₂O₁₅ is shown in the insets image. Compared with the common [Bi₂O₂] slabs layer structure in BiOX and Bi₂WO₆ [17,18], the key structural elements of unit cell Bi₆S₂O₁₅ are (Bi₁₂O₁₄)_n⁸⁺ columns extending along the *c* axis that are surrounded by eight SO₄²⁻ tetrahedral. The formation of Bi₆S₂O₁₅ nanowires may originate from the inherent structural anisotropy arising from the linear arrangement of (Bi₁₂O₁₄)_n⁸⁺ columns [19]. Two different Bi can be found in a unit cell: the [BiO₆] unit with only Bi–O–Bi bonds and the [BiO₃] unit with Bi–O–Bi and Bi–O–S bonds. In this case, the formation of bismuth defects shell may be due to the transformation from [BiO₆] to [BiO₃] unit in the surface crystal, which will be further discussed in the following.

Fig. S5 shows the scanning electron microscopy (SEM) images of the pure Bi₆S₂O₁₅ and vacancy Bi₆S₂O₁₅ nanowires samples. The as-synthesis pure Bi₆S₂O₁₅ and vacancy Bi₆S₂O₁₅ samples are wire-

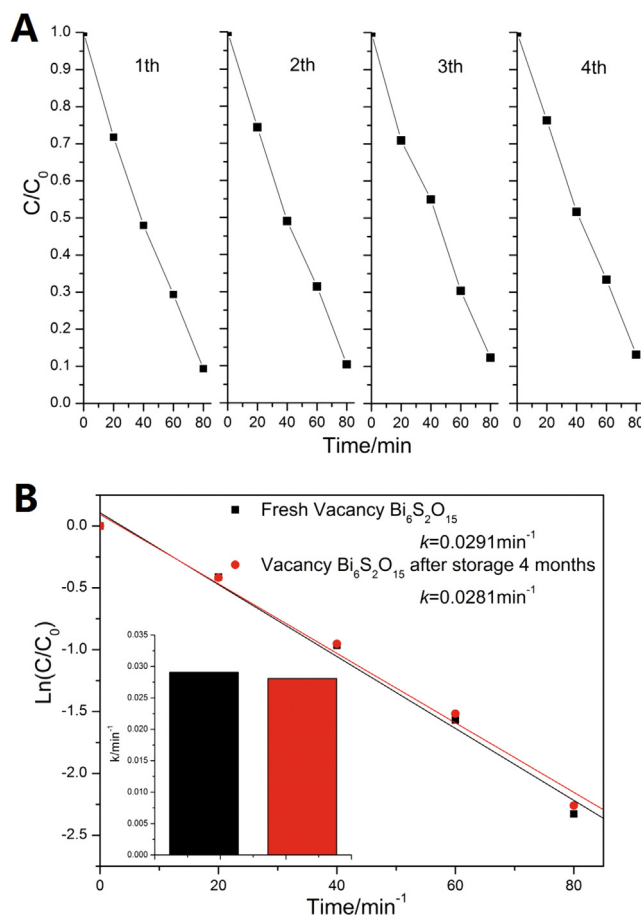


Fig. 5. (A) Cycling runs in the photodegradation of MB in the presence of vacancy Bi₆S₂O₁₅ nanowires under UV light ($\lambda = 254 \text{ nm}$). (B) UV photocatalytic activities of fresh and after storage 4 months vacancy Bi₆S₂O₁₅ nanowires on the degradation of MB.

like nanostructures with diameter about 60 nm and the length more than tens of micrometers, which virtually corresponds to an aspect ratio of greater than 100. The morphology is not changed for the Bi₆S₂O₁₅ with and without surface bismuth defects.

To further investigate the defect structure, the HRTEM images of pure Bi₆S₂O₁₅ and vacancy Bi₆S₂O₁₅ nanowires samples are presented as shown in Fig. 6A and B. Fig. 6A is the border image observed over $[-714]$ zone axis from a single pure Bi₆S₂O₁₅ nanowires. According to the images, the pure Bi₆S₂O₁₅ nanowires sample displays perfect lattice features in most areas. The lattice spacing of two lattice fringes is 0.27 nm and 0.41 nm, corresponding to that of (1 7 0) and (1 3 1) planes of Bi₆S₂O₁₅. The pure Bi₆S₂O₁₅ nanowires display oriented growth along the [0 0 1] direction (*c* axis), which is further confirmed in the Fig. S6. Although a thin and irregular disordered shell can be observed in the image. We tentatively consider that the thinner disordered structures are mainly attributed to the lack of diffraction conditions rather than the formation of surface bismuth defects. As shown in Fig. S7 SEM image, it is clear that the cross section of the nanowires is parallelogram. Thus, the edge of nanowires is too thin to collect enough diffraction signal.

In vacancy Bi₆S₂O₁₅ nanowires system, as shown in Fig. 6B, the nanowire can be divided into two parts: internal crystalline core and external disorder shell. The lattice spacing of internal three lattice fringes are 0.30 nm, 1.03 nm, and 0.50 nm, corresponding to the (3 3 1), (1 1 0), and (1 1 1) planes of Bi₆S₂O₁₅. The thickness of defect shell is about 5.1 nm. We tentatively conjecture that the

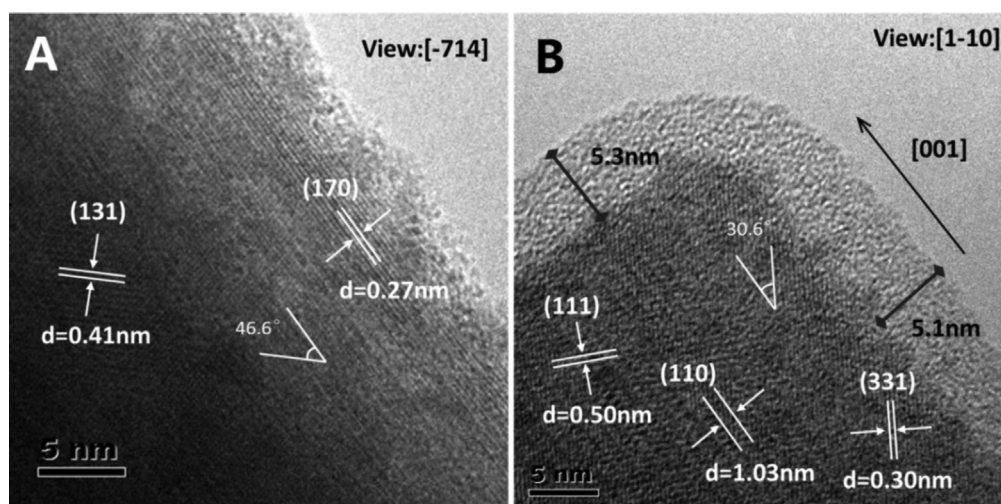


Fig. 6. HR-TEM images of pure $\text{Bi}_6\text{S}_2\text{O}_{15}$ nanowires (A) and vacancy $\text{Bi}_6\text{S}_2\text{O}_{15}$ nanowires (B) samples.

formation of defect layer is attributed to the lack of Bi element, which will be further discussed in the following.

To further understand the defect structure, the energy dispersive spectra (EDS) and XPS surface elements analysis are performed to detect the Bi and S atoms in the pure $\text{Bi}_6\text{S}_2\text{O}_{15}$ and vacancy $\text{Bi}_6\text{S}_2\text{O}_{15}$ nanowires samples. In the EDS elemental mappings (Fig. S8), the ratio of Bi to S for single nanowire of vacancy $\text{Bi}_6\text{S}_2\text{O}_{15}$ nanowires sample is 2.68, which is slightly lower than that of pure $\text{Bi}_6\text{S}_2\text{O}_{15}$ (2.87). The element line/point scan has been performed to further investigate the difference in chemical compositions along the vacancy $\text{Bi}_6\text{S}_2\text{O}_{15}$ nanowire (Fig. S9). The element line scan results show that element of Bi and S decrease obviously in the area of surface vacancy. The element point scan results show that the ratio of Bi to S for surface vacancy (Spectrogram 29) is only 0.85, which is greatly lower than that of body area (Spectrogram 30, 3.19). Moreover, in the XPS surface elements analysis of the pure $\text{Bi}_6\text{S}_2\text{O}_{15}$ and vacancy $\text{Bi}_6\text{S}_2\text{O}_{15}$ nanowires, an obviously decrease in the ratio of Bi to S can be observed as shown in Table 1, where the ratio of Bi to S for vacancy $\text{Bi}_6\text{S}_2\text{O}_{15}$ nanowires is 2.18, which has a great deviation from the stoichiometric ratio (3.00). As a surface analysis method, the XPS analysis is mainly focused on the surface atoms layer with the depth about 5 nm, which fits well with

Table 1

XPS surface elements analysis of the pure $\text{Bi}_6\text{S}_2\text{O}_{15}$ and vacancy $\text{Bi}_6\text{S}_2\text{O}_{15}$ nanowires.

Samples	S%	Bi%	Bi:S
Pure $\text{Bi}_6\text{S}_2\text{O}_{15}$	1.52	4.46	2.93:1
Vacancy $\text{Bi}_6\text{S}_2\text{O}_{15}$	9.01	19.69	2.18:1

the defect shell. These results indicate that the formation of defect shell in vacancy $\text{Bi}_6\text{S}_2\text{O}_{15}$ nanowires is attributed to the lack of Bi element.

Raman spectroscopy is a much more sensitive technique for the examination of the nanosized crystalline domain. Fig. S10A shows the Raman scattering spectrum of the pure $\text{Bi}_6\text{S}_2\text{O}_{15}$ and vacancy $\text{Bi}_6\text{S}_2\text{O}_{15}$ nanowires samples, obtained in ambient atmosphere with an excitation wavelength of 514 nm, which contains a low frequency region ranging from 60 to 700 cm^{-1} . The Raman peaks occur in the region below 120 cm^{-1} denote the presence of the Bi^{3+} cations as $[\text{BiO}_3]$ and $[\text{BiO}_6]$ polyhedra [20]. The two first-order Raman modes at 70 and 99 cm^{-1} are assigned respectively, to the Eg and A1g vibration modes of Bi [21]. In the region from 120 to 400 cm^{-1} , the Raman peaks are expected to be due to the Bi–O stretches of $[\text{BiO}_6]$ polyhedral [20,22]. The triply degenerate

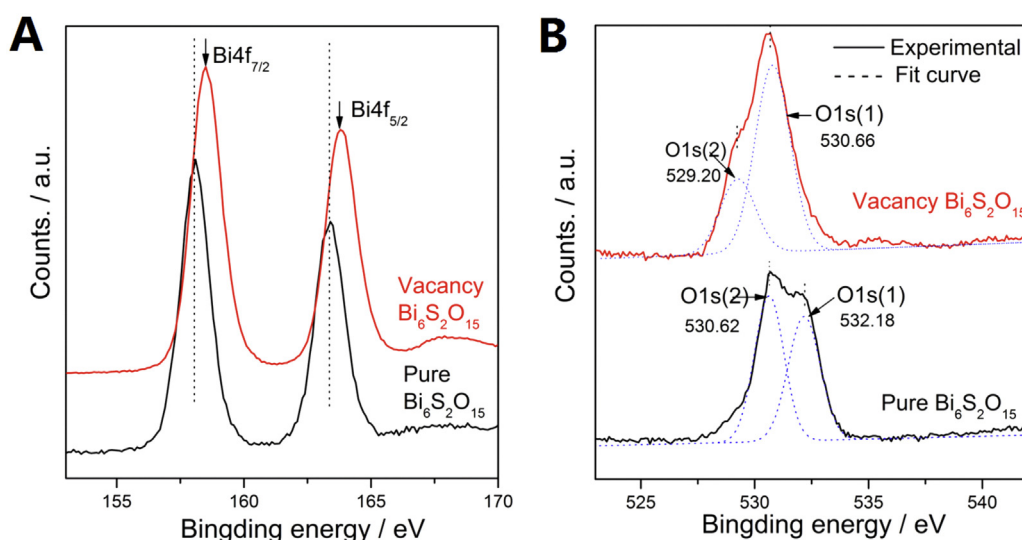


Fig. 7. XPS Spectrum of pure $\text{Bi}_6\text{S}_2\text{O}_{15}$ and vacancy $\text{Bi}_6\text{S}_2\text{O}_{15}$ nanowires samples; (A) Bi 4f photoelectron spectra for pure $\text{Bi}_6\text{S}_2\text{O}_{15}$ and vacancy $\text{Bi}_6\text{S}_2\text{O}_{15}$ nanowires; and (B) experimental and decomposed peaks of O 1s photoelectron spectra of pure $\text{Bi}_6\text{S}_2\text{O}_{15}$ and vacancy $\text{Bi}_6\text{S}_2\text{O}_{15}$ nanowires.

v2(E) bending mode and v4(T2) vibrational modes of the SO_4^{2-} are observed as a triplet at 432, 441, and 476 cm^{-1} , and three corresponding Raman-active vibrations at 584, 607 and 626 cm^{-1} , respectively [16]. No significant change in Raman scattering spectrum of the pure $\text{Bi}_6\text{S}_2\text{O}_{15}$ and vacancy $\text{Bi}_6\text{S}_2\text{O}_{15}$ nanowires can be found, indicating that no transformation occurs in the crystal phase structures, which is in good agreement with the XRD. However, obvious changes in relative intensity of Raman peaks can be observed. The relative intensity of Bi^{3+} cations peaks for vacancy $\text{Bi}_6\text{S}_2\text{O}_{15}$ nanowires are obviously higher than that of pure $\text{Bi}_6\text{S}_2\text{O}_{15}$, while a slightly decrease can be found in the relative intensity of $[\text{BiO}_6]$ polyhedral peaks (Fig. S10A insets). These results indicate that, compared to pure $\text{Bi}_6\text{S}_2\text{O}_{15}$, the ratio of $[\text{BiO}_3]$ to $[\text{BiO}_6]$ has increased in vacancy $\text{Bi}_6\text{S}_2\text{O}_{15}$ nanowires, which can be further confirmed by the FT-IR as shown in Fig. S10B insets [23]. The relative intensity of $[\text{BiO}_3]$ characteristic vibration in 830 cm^{-1} for vacancy $\text{Bi}_6\text{S}_2\text{O}_{15}$ nanowires is about 4 times as large as that of pure $\text{Bi}_6\text{S}_2\text{O}_{15}$. What is more, the vibration of hydroxide radical defects in 1413, 1641, 3514, and 3868 cm^{-1} can be found in the vacancy $\text{Bi}_6\text{S}_2\text{O}_{15}$ nanowires sample (Fig. S10B) [24]. Typically, hydroxide radical defects can be differentiate into two parts: one is in the lattice distortion where H^+ combined with O atom; the other is in the form of the OH groups absorbed on the surface as it generally does in TiO_2 . In this case, we tentatively conjecture that the formation of hydroxide radical defects is attributed to the lattice distortion caused by surface bismuth-vacancy. The surface hydroxide radical defects benefit for the production of hydroxyl radicals ($\cdot\text{OH}$), which will be further discussed below.

Bi 4f and O 1s X-ray photoelectron spectroscopy (XPS) results of the pure $\text{Bi}_6\text{S}_2\text{O}_{15}$ and vacancy $\text{Bi}_6\text{S}_2\text{O}_{15}$ nanowires samples are shown in Fig. 7. Compared to the pure $\text{Bi}_6\text{S}_2\text{O}_{15}$, the Bi 4f photoelectron peaks of vacancy $\text{Bi}_6\text{S}_2\text{O}_{15}$ nanowires shift to higher binding energy with the formation of surface bismuth defects (Fig. 7A). It indicates that the average electron density of Bi–O. Furthermore, the binding energy of O 1s for vacancy $\text{Bi}_6\text{S}_2\text{O}_{15}$ nanowires is about 530.5 eV, which is slightly smaller than that of pure $\text{Bi}_6\text{S}_2\text{O}_{15}$ (531.5 eV) (Fig. 7B). This shift may be attributed to weakness of the hybridization between Bi6s and O 2p as a result from the introduction of surface bismuth defects. The O 1s peak can be fitted to decompose the asymmetric peaks by a sum of Gaussian curves by means of least square method. The peak O 1s(2) at lower energy is attributed to the oxygen atoms linked to the cations with lower electronegativity (such as O–Bi) and non-bridging oxygen. The peak O 1s(1) at higher energy belongs to the oxygen atoms bonded to higher electronegativity cations (such as O–S) and bridging oxygen [25,26]. It is found that the intensity of O 1s(2) decreases with the formation of surface bismuth defects, while that of O 1s(1) increases. It suggests that the average cation–oxygen bond (Bi–O) binding energy decreases as the surface bismuth defects form. As mentioned above, two different Bi can be found in a unit cell: the $[\text{BiO}_6]$ unit with only Bi–O–Bi bonds and the $[\text{BiO}_3]$ unit with Bi–O–Bi and Bi–O–S bonds. In this case, the ratio of $[\text{BiO}_3]$ to $[\text{BiO}_6]$ increases as the bismuth defects form on the crystal surface. In other word, the ratio of Bi–O–S to Bi–O–Bi bonds in vacancy $\text{Bi}_6\text{S}_2\text{O}_{15}$ nanowires is higher than that of pure $\text{Bi}_6\text{S}_2\text{O}_{15}$.

Based on the results above, the disorder shell on the vacancy $\text{Bi}_6\text{S}_2\text{O}_{15}$ nanowires is demonstrated to be surface bismuth defects, which is resulted from the transition from $[\text{BiO}_6]$ unit with only Bi–O–Bi bonds into the $[\text{BiO}_3]$ with Bi–O–Bi and Bi–O–S bonds in the crystal surface.

3.3. Mechanism of enhancement of photocatalytic activity

It is well known that photocatalytic activity is governed by various factors such as crystal phase structure, surface area, band gap

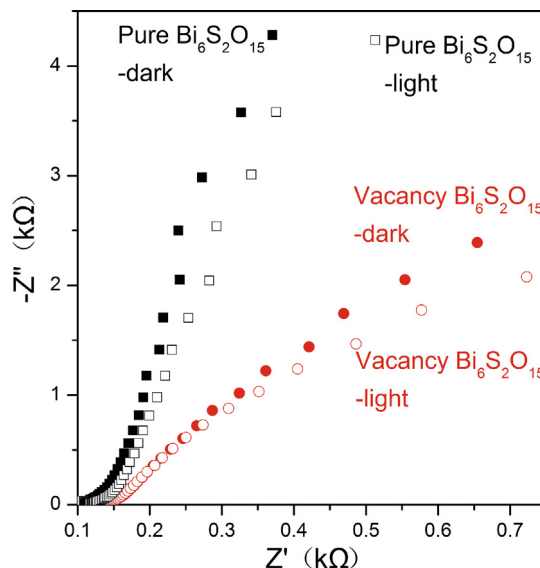


Fig. 8. Electrochemical impedance spectroscopy (EIS) Nyquist plots of pure $\text{Bi}_6\text{S}_2\text{O}_{15}$ and vacancy $\text{Bi}_6\text{S}_2\text{O}_{15}$ nanowires electrodes under UV light irradiation.

and separation efficiency of photoinduced electrons and holes [27]. As mentioned above, the crystal phase structures are not changed for $\text{Bi}_6\text{S}_2\text{O}_{15}$ with and without surface bismuth defects (Fig. 6). Moreover, the BET surface area of pure $\text{Bi}_6\text{S}_2\text{O}_{15}$ and vacancy $\text{Bi}_6\text{S}_2\text{O}_{15}$ nanowires (Table S2) are $12.97\text{ m}^2/\text{g}^{-1}$ and $10.58\text{ m}^2/\text{g}^{-1}$, respectively. It is noted that activity decreasing order is just opposite to BET surface area of pure $\text{Bi}_6\text{S}_2\text{O}_{15}$ and vacancy $\text{Bi}_6\text{S}_2\text{O}_{15}$ nanowires. This implies that the photocatalytic activity difference among pure $\text{Bi}_6\text{S}_2\text{O}_{15}$ and vacancy $\text{Bi}_6\text{S}_2\text{O}_{15}$ nanowires is not due to the crystal phase structure and physical adsorption.

The separation efficiency of photoinduced electron–hole pairs can be investigated by the electrochemical impedance spectra (EIS) [28]. In the EIS mappings (Fig. 8), the diameter of the pure $\text{Bi}_6\text{S}_2\text{O}_{15}$ and vacancy $\text{Bi}_6\text{S}_2\text{O}_{15}$ nanowires electrodes semicircle tends to obviously decrease under UV illumination due to the large increase of the charge transfer and the separation of the electron–hole pairs. The arc radius of vacancy $\text{Bi}_6\text{S}_2\text{O}_{15}$ nanowires electrode is smaller than that of pure $\text{Bi}_6\text{S}_2\text{O}_{15}$ electrode. The smaller the arc radius of an EIS Nyquist plot, the higher the efficiency of charge separation [29]. Therefore, the enhancement of the photocatalytic performance is resulted from the improvement of the charge separation efficiency due to the bandgap narrowing induced by surface bismuth-vacancy states, which will be discussed in the following.

To elucidate the photocatalytic mechanism of the pure $\text{Bi}_6\text{S}_2\text{O}_{15}$ and vacancy $\text{Bi}_6\text{S}_2\text{O}_{15}$ nanowires, the trapping experiments is performed to detect main oxidative species (radicals and holes) in the photocatalytic process. The holes (h^+), hydroxyl radicals ($\cdot\text{OH}$) and superoxide radical ($\cdot\text{O}_2^-$) during the photodegradation of MB over pure $\text{Bi}_6\text{S}_2\text{O}_{15}$ and vacancy $\text{Bi}_6\text{S}_2\text{O}_{15}$ nanowires are investigated with the addition of HCOOH (holes scavenger) [30], *t*-BuOH (hydroxyl radicals scavenger) [31], and *p*-benzoquinone (superoxide radicals scavenger) [32], as shown in Fig. 9A and B. In pure $\text{Bi}_6\text{S}_2\text{O}_{15}$ system, the addition of *t*-BuOH and *p*-benzoquinone only cause a small change in the photocatalytic degradation of MB. On the contrary, the photodegradation rate is greatly decreased with the addition of a scavenger for holes (HCOOH), indicating that the photogenerated holes are the main oxidative species of pure $\text{Bi}_6\text{S}_2\text{O}_{15}$ (Fig. 9A). In vacancy $\text{Bi}_6\text{S}_2\text{O}_{15}$ nanowires system (Fig. 9B), the photocatalytic degradation rate is slightly suppressed by the addition of HCOOH, while it is obviously inhibited when the superoxide radicals (*p*-benzoquinone) and hydroxyl radicals scavenger (*t*-BuOH) added. These results suggest that the main oxidative

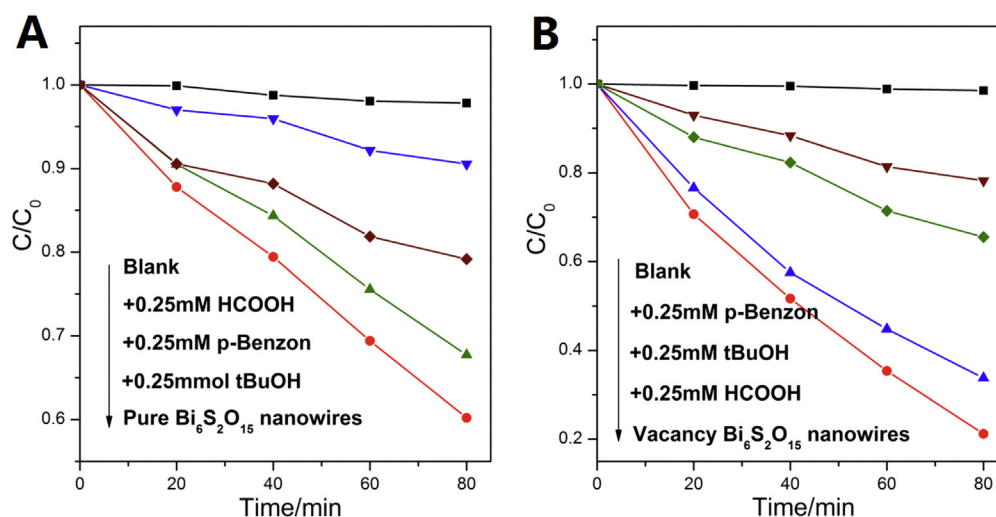


Fig. 9. The plots of photogenerated carriers trapping in the system of photodegradation of MB by (A) pure $\text{Bi}_6\text{S}_2\text{O}_{15}$ nanowires and (B) vacancy $\text{Bi}_6\text{S}_2\text{O}_{15}$ nanowires, under UV light, respectively.

species of photocatalysts transform from holes (h^+) to the superoxide radical ($\cdot\text{O}_2^-$) and hydroxyl radicals ($\cdot\text{OH}$) as the bismuth defects form in the shell.

In general, the high redox potential of photogenerated holes and electrons benefits for the production of active oxidative species, which is conducive to photocatalytic activity. The positions of the valence and conduction bands are estimated by the UV–vis diffuse reflectance spectra and Mott–Schottky plots.

The UV–vis diffuse reflectance spectra of pure $\text{Bi}_6\text{S}_2\text{O}_{15}$ and vacancy $\text{Bi}_6\text{S}_2\text{O}_{15}$ nanowires have been discussed above. The main band-gap energy of pure $\text{Bi}_6\text{S}_2\text{O}_{15}$ and vacancy $\text{Bi}_6\text{S}_2\text{O}_{15}$ nanowires is estimated to be 3.35 eV. The surface defects absorption edge of vacancy $\text{Bi}_6\text{S}_2\text{O}_{15}$ nanowires occurs at about 450 nm and the corresponding band-gap energy is estimated to be 2.76 eV. Furthermore, the bottom of conduction band for pure $\text{Bi}_6\text{S}_2\text{O}_{15}$ and vacancy $\text{Bi}_6\text{S}_2\text{O}_{15}$ nanowires can be estimated by the Mott–Schottky plots. It can be calculated through the following equation: $\Delta E = \text{ECB} - \text{EFb}$ where ΔE is assumed to be -0.3 V due to the similar composition and insulating n -type semiconducting properties [33]. As shown in Fig. 10A, two different frequencies were performed to ensure the accuracy of experimental results. The flat band potential for

pure $\text{Bi}_6\text{S}_2\text{O}_{15}$ and vacancy $\text{Bi}_6\text{S}_2\text{O}_{15}$ nanowires is -1.50 V , -1.84 V vs. SCE, respectively. As a result, the potential of conductive bands of vacancy $\text{Bi}_6\text{S}_2\text{O}_{15}$ nanowires is about -2.14 V vs. SCE, which is 0.34 V higher than that of pure $\text{Bi}_6\text{S}_2\text{O}_{15}$ (-1.80 V). Combining with the band gap, the oxidation potential in the valence band for pure $\text{Bi}_6\text{S}_2\text{O}_{15}$ and vacancy $\text{Bi}_6\text{S}_2\text{O}_{15}$ nanowires estimated to be 1.55 V , 0.62 V vs. SCE, respectively.

Based on the results above, a schematic diagram for the density of states (DOS) of pure $\text{Bi}_6\text{S}_2\text{O}_{15}$ and vacancy $\text{Bi}_6\text{S}_2\text{O}_{15}$ nanowires has been proposed as shown in Fig. 10B. The forbidden gap of pure $\text{Bi}_6\text{S}_2\text{O}_{15}$ is about 3.35 eV, which can only absorb light wavelength less than 370 nm. In previous work, the introduction of surface oxygen vacancies in several semiconductors (TiO_2 , ZnO , and BiPO_4) is demonstrated to be conducive to band gap narrowing and photoactivity. However, the surface vacancy states reported in these researches generally occur only above the valence band maximum (VBM). Compared to the surface oxygen vacancies, the introduction of surface bismuth vacancies in our research elevated whole bands and many shallow surface bismuth-vacancy states appear above and partly overlapping with the VB. As a result, the conduction-

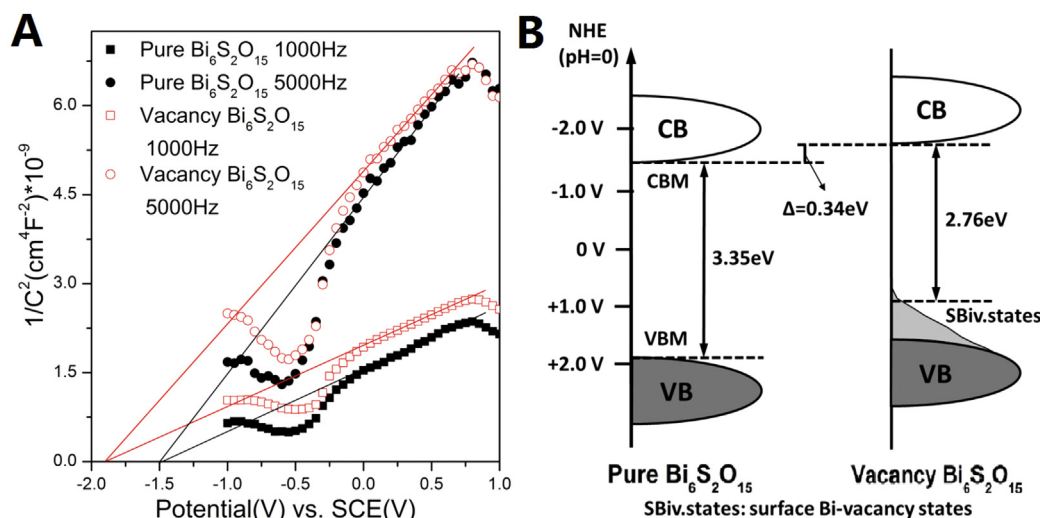


Fig. 10. (A) Mott–Schottky plots of pure $\text{Bi}_6\text{S}_2\text{O}_{15}$ and vacancy $\text{Bi}_6\text{S}_2\text{O}_{15}$ nanowires samples; counter electrode: Pt; electrolyte: $0.1 \text{ M Na}_2\text{SO}_4$, frequency: 1 kHz and 5 kHz ; and (B) schematic diagram illustrating the density of states (DOS) of pure $\text{Bi}_6\text{S}_2\text{O}_{15}$ and vacancy $\text{Bi}_6\text{S}_2\text{O}_{15}$ nanowires.

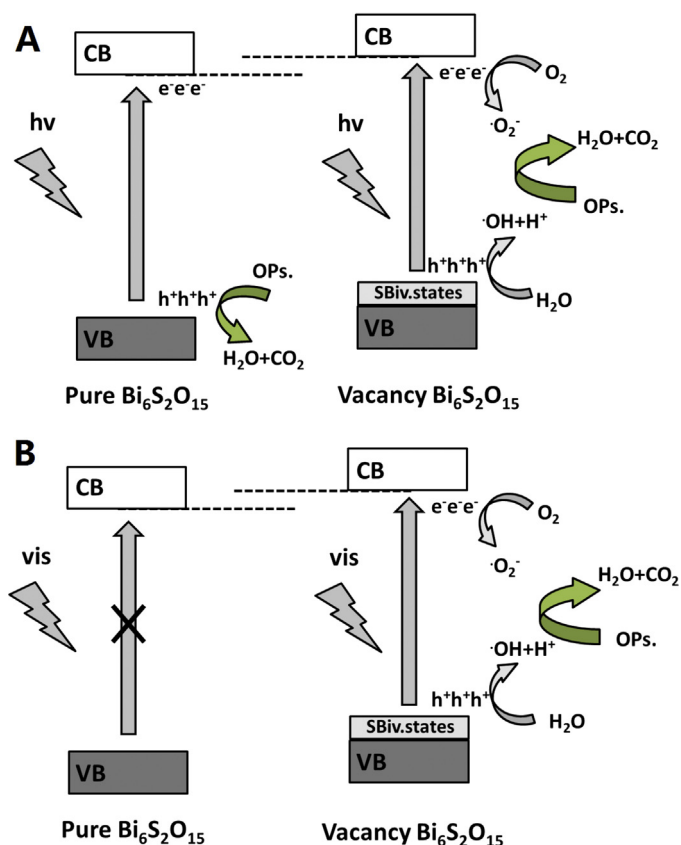


Fig. 11. The mechanism of charge separation and photocatalytic reaction of pure $\text{Bi}_6\text{S}_2\text{O}_{15}$ and vacancy $\text{Bi}_6\text{S}_2\text{O}_{15}$ nanowires photocatalysts under UV (A) and visible light (B).

band minimum (CBM) and valence-band maximum (VBM) are raised by 0.34 eV and 0.93 eV, respectively.

The proposed schematic for UV and visible photocatalytic reaction and electron-hole separation process of pure $\text{Bi}_6\text{S}_2\text{O}_{15}$ and vacancy $\text{Bi}_6\text{S}_2\text{O}_{15}$ nanowires photocatalysts are shown in Fig. 11. Surface bismuth vacancies elevate the whole bands and introduce impurity states above the valence band. Compared to the pure $\text{Bi}_6\text{S}_2\text{O}_{15}$, vacancy $\text{Bi}_6\text{S}_2\text{O}_{15}$ nanowires has higher CBM and a lower VBM, which results in the transition of main oxidative species from holes (h^+) to the superoxide radical ($\cdot\text{O}_2^-$) and hydroxyl radicals ($\cdot\text{OH}$) (Fig. 11A). The high reduction potential of photogenerated electrons benefits for the production of active superoxide radical, which is conducive to photocatalytic activity. What is more, the introduction of surface bismuth-vacancy states can expand the VB width, which contributes to increasing the separation efficiency of photoinduced electron-hole pairs, leading to enhancement of the photocatalytic activity. More interesting, pure $\text{Bi}_6\text{S}_2\text{O}_{15}$ itself cannot be excited by visible light. The generation of visible activity is attributed to the narrow of energy band gap due to the rise of VBM (Fig. 11B).

4. Conclusion

The core/shell structured $\text{Bi}_6\text{S}_2\text{O}_{15}$ nanowires with surface bismuth defects have been synthesized. The vacancy $\text{Bi}_6\text{S}_2\text{O}_{15}$

nanowires exhibit vastly superior photocatalytic activity than pure $\text{Bi}_6\text{S}_2\text{O}_{15}$. Surface bismuth defects can elevate the conduction band and decrease the band gap by introducing the impurity states above the valence band. The main oxidative species of photocatalysts transform from holes (h^+) to the superoxide radical ($\cdot\text{O}_2^-$) and hydroxyl radicals ($\cdot\text{OH}$). The photocatalytic performance is obviously improved owing to the high charge separation efficiency.

Acknowledgments

This work was partly supported by National Basic Research Program of China (2013CB632403), National High Technology Research and Development Program of China (2012AA062701) and Chinese National Science Foundation (21373121).

Appendix A. Supplementary data

Supplementary data associated with this article can be found, in the online version, at <http://dx.doi.org/10.1016/j.apcatb.2015.04.022>.

References

- [1] X. Chen, S.S. Mao, Chem. Rev. 107 (2007) 2891–2959.
- [2] V. Etacheri, M.K. Seery, S.J. Hinder, S.C. Pillai, Chem. Mater. 22 (2010) 3843–3853.
- [3] L. Zhang, Y. Zhu, Catal. Sci. Technol. 2 (2012) 694–706.
- [4] J. Tang, J.R. Durrant, D.R. Klug, J. Am. Chem. Soc. 130 (2008) 13885–13891.
- [5] X. Chen, L. Liu, Y.Y. Peter, S.S. Mao, Science 331 (2011) 746–750.
- [6] G. Liu, L. Wang, H.G. Yang, H.-M. Cheng, G.Q.M. Lu, J. Mater. Chem. 20 (2010) 831–843.
- [7] M.R. Hoffmann, S.T. Martin, W. Choi, D.W. Bahnemann, Chem. Rev. 95 (1995) 69–96.
- [8] W. Choi, A. Termin, M.R. Hoffmann, J. Phys. Chem. 98 (1994) 13669–13679.
- [9] M. Kong, Y. Li, X. Chen, T. Tian, P. Fang, F. Zheng, X. Zhao, J. Am. Chem. Soc. 133 (2011) 16414–16417.
- [10] H. Cheng, A. Selloni, Phys. Rev. B. 79 (2009) 092101.
- [11] A. Naldoni, M. Allietta, S. Santangelo, M. Marelli, F. Fabbri, S. Cappelli, C.L. Bianchi, R. Psaro, V. Dal Santo, J. Am. Chem. Soc. 134 (2012) 7600–7603.
- [12] Y. Lv, C. Pan, X. Ma, R. Zong, X. Bai, Y. Zhu, Appl. Catal. B 138 (2013) 26–32.
- [13] Y. Lv, Y. Zhu, Y. Zhu, J. Phys. Chem. C 117 (2013) 18520–18528.
- [14] Y. Lv, Y. Liu, Y. Zhu, Y. Zhu, J. Mater. Chem. 2 (2014) 1174–1182.
- [15] Y. Lv, Y. Zhu, Y. Zhu, J. Phys. Chem. C 117 (2013) 18520–18528.
- [16] Y. Zhou, J.D. Grunwaldt, F. Krumeich, K. Zheng, G. Chen, J. Stötzler, R. Frahm, G.R. Patzke, Small 6 (2010) 1173–1179.
- [17] A. Taoufyq, H. Ait Ahsaine, L. Patout, A. Benlhamchi, M. Ezahri, F. Guinneton, A. Lyoussi, G. Nolibe, J.R. Gavarri, J. Solid State Chem. 203 (2013) 8–18.
- [18] L. Ye, L. Zan, L. Tian, T. Peng, J. Zhang, Chem. Commun. 47 (2011) 6951–6953.
- [19] Y. Zhou, G.R. Patzke, CrystEngComm 14 (2012) 1161–1163.
- [20] L. Kumari, J.-H. Lin, Y.-R. Ma, J. Phys.: Condens. Matter 19 (2007) 406204.
- [21] F.D. Hardcastle, I.E. Wachs, J. Solid State Chem. 97 (1992) 319–331.
- [22] L. Baia, R. Stefan, J. Popp, S. Simon, W. Kiefer, J. Non-Cryst. Solids 324 (2003) 109–117.
- [23] I. Ardelean, S. Cora, J. Mater. Sci. – Mater. Electron. 19 (2008) 584–588.
- [24] C. Pan, J. Xu, Y. Chen, Y. Zhu, Appl. Catal. B 115 (2012) 314–319.
- [25] H. Fan, G. Gao, G. Wang, L. Hu, Solid State Sci. 12 (2010) 541–545.
- [26] H. Fan, G. Wang, L. Hu, Solid State Sci. 11 (2009) 2065–2070.
- [27] S. Zhu, T. Xu, H. Fu, J. Zhao, Y. Zhu, Environ. Sci. Technol. 41 (2007) 6234–6239.
- [28] Z. Hosseini, N. Taghavinia, N. Sharifi, M. Chavoshi, M. Rahman, J. Phys. Chem. C 112 (2008) 18686–18689.
- [29] C. Pan, D. Li, X. Ma, Y. Chen, Y. Zhu, Catal. Sci. Technol. 1 (2011) 1399–1405.
- [30] T. Tan, D. Beydoun, R. Amal, J. Photochem. Photobiol. A 159 (2003) 273–280.
- [31] H. Lee, W. Choi, Environ. Sci. Technol. 36 (2002) 3872–3878.
- [32] W. Liu, M. Wang, C. Xu, S. Chen, X. Fu, J. Mol. Catal. A – Chem. 368–369 (2013) 9–15.
- [33] K. Ogisu, A. Ishikawa, Y. Shimodaira, T. Takata, H. Kobayashi, K. Domen, J. Phys. Chem. C 112 (2008) 11978–11984.